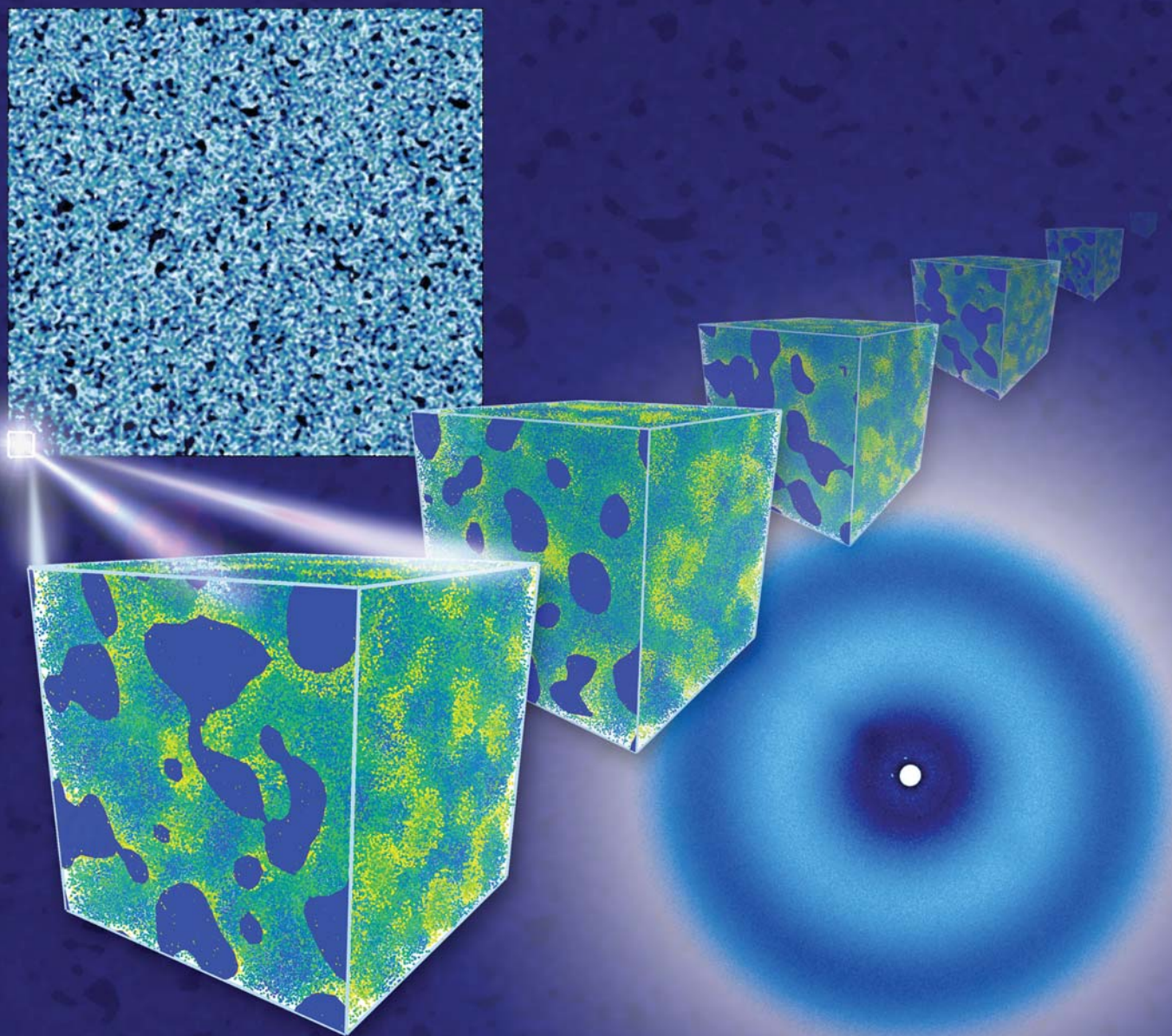


Soft Matter

www.rsc.org/softmatter

Volume 7 | Number 15 | 7 August 2011 | Pages 6729–7124



ISSN 1744-683X

RSC Publishing

PAPER

James A. Elliott *et al.*

A unified morphological description of Nafion membranes from SAXS and mesoscale simulations

Cite this: *Soft Matter*, 2011, **7**, 6820

www.rsc.org/softmatter

PAPER

A unified morphological description of Nafion membranes from SAXS and mesoscale simulations

James A. Elliott,^{*a} Dongsheng Wu,^b Stephen J. Paddison^b and Robert B. Moore^c

Received 3rd January 2011, Accepted 8th April 2011

DOI: 10.1039/c1sm00002k

Although many different structural models have been proposed for perfluorosulfonic acid (PFSA) ionomers such as Nafion, the very high degree of disorder in these materials makes it difficult, if not impossible, to deduce their morphology unambiguously from small angle X-ray and neutron scattering (SAXS/SANS) experiments alone. We present a combination of a model-independent procedure for obtaining structural information from SAXS patterns based on a Maximum Entropy (MaxEnt) approach coupled with mesoscale simulations of the morphology of Nafion using Dissipative Particle Dynamics (DPD) parameterized with atomistic calculations and density functional theory. These two methods show that the nanoscale ionic clustering in PFSA is intimately linked to, but spatially separate from, the larger scale organization of the fluorocarbon backbone. Although we are unable to directly observe crystallization of the backbone in the DPD simulations, the high density regions of fluorocarbon segments correspond exactly to those regions where the density of ionic clusters is lowest, each forming an independent bicontinuous domain. We are thus able to demonstrate a unified morphological description of PFSA based on both statistical (MaxEnt) and thermodynamic (DPD) descriptions, which broadly favours a bicontinuous network of ionic clusters embedded in a matrix of fluorocarbon chains.

1 Introduction

Due to the widespread use of perfluorosulfonic acid (PFSA) ionomers,¹ such as Nafion, in proton exchange membrane (PEM) fuel cells² and other redox applications,³ many different structural models have been proposed in order to explain the effect of membrane morphology on properties such as the water swelling behaviour and proton transport.^{4–6} There is widespread agreement that this arises due to the phase separation of the sulfonate side groups and aqueous counterions from the polytetrafluoroethylene (PTFE) backbone. However, a detailed understanding of the phase-separated morphology of PFSA ionomers at the nanoscale is crucial to enable the design of new materials, including non-fluorinated^{4,7} or composite membranes,^{3,8,9} which may yield improved performance in fuel cells operating at high temperatures or low water contents. The phenomenon of proton transport in nanoscale confined geometries^{10,11} is also relevant to

many other soft matter systems, such as water wires in carbon nanotubes¹² and proton channels in biological membranes.¹³

One of the earliest structural models for PFSA ionomers was the cluster-network model of Hsu and Gierke,^{14,15} who proposed the existence of spherical domains of water-rich sulfonic acid phase, connected by narrow channels and embedded in an amorphous fluorocarbon matrix, which swell on addition of water to the membrane. Although this model gives a phenomenological rationalization for the selective ionic conductivity of Nafion, and provides a qualitative explanation of the “ionomer” peak in small-angle X-ray scattering (SAXS) data, it has since been shown to be quantitatively inconsistent with data over a wider range of scattering angles^{16,17} and from membranes oriented by tensile draw.¹⁸ Furthermore, it takes no account of crystallinity in the fluorocarbon phase¹⁹ and is not compatible with the inverse micellar structure of Nafion aggregates dissolved in solution.^{20,21}

As an alternative, Gebel, Diat and co-workers proposed the fibrillar or polymeric bundle model,¹⁶ consisting of fluorocarbon chains surrounded by ionic groups and water, which rotate and then orient under uniaxial stretching.²⁰ The scattering behaviour at low scattering vector, q , resembles a q^{-1} power law predicted for independent, randomly oriented cylinders.²² On addition of water, swelling occurs *between* aggregates, as opposed to the cluster-network model in which there is swelling *of* the aggregates themselves. The fibrillar model can also be applied to Nafion in solution (a polyelectrolyte as opposed to a polymer electrolyte),

^aDepartment of Materials Science and Metallurgy, University of Cambridge, Pembroke Street, Cambridge, CB2 3QZ, UK. E-mail: jae1001@cam.ac.uk; Tel: +44 (0)1223 335987

^bDepartment of Chemical and Biomolecular Engineering, University of Tennessee, Knoxville, TN, 37996, USA

^cMacromolecules and Interfaces Institute, Department of Chemistry, Virginia Polytechnic Institute and State University, Blacksburg, Virginia, 24061, USA

since it was developed with the whole solvent concentration range in mind;^{23–26} however, it may understate the degree of structural reorganization that can take place during swelling. The lengths of the cylindrical domains were estimated to be in excess of 80–100 nm, compared to contour lengths of 175–1750 nm for Nafion with a molecular weight of between 10^5 and 10^6 g mol⁻¹,²⁷ and would thus require substantially chain-extended crystallites. Furthermore, given persistence lengths of 3–5 nm for per-fluoroalkanes,^{28,29} there is no symmetry-breaking mechanism to account for the global alignment of chains into cylinders in the absence of any externally applied field or mechanical stress. Nevertheless, the effects of tensile draw on SAXS data can be explained in terms of orientation of fibrillar bundles,³⁰ and they give a natural explanation for the presence of fluorocarbon crystallites which are important in physically cross-linking the membrane.

More recently, Schmidt-Rohr and Chen have proposed the parallel cylinder model,¹⁷ based on simulation of SAXS curves using numerical Fourier transform techniques.³¹ Their model contained large fluorocarbon crystallites, existing independently of ionic aggregates, which themselves consisted of long parallel cylinders decorated internally with ionic groups and water. They argued that the combination of a q^{-1} power law regime at low q , together with the absence of a meridional component of the ionomer peak in oriented Nafion,^{32,33} necessarily implies a cylindrical morphology. However, in fact, correctly reproducing the X-ray scattering data is only a necessary and not sufficient constraint on the morphology due to the non-uniqueness caused by neglect of phase information. Furthermore, the parallel cylinder model also requires extreme lengths for the PTFE crystallites and water channels (greater than 100 nm), which was justified by the stabilization due to the high stiffness of the PTFE backbone.³⁴ As in the fibrillar bundle model, the mechanism of symmetry-breaking for formation of cylinders is never explained, and there is no account of structural reorganization required to explain the non-affine swelling behaviour with increasing water content.³⁵ In order to obtain a more fundamental evaluation of PFSA morphology, in particular the relative thermodynamic stability of various models, it is helpful to employ computational simulation techniques based on rigorous statistical mechanics approaches.

Beginning in the mid-1990s, there have been a number of classical atomistic,^{36–40} quantum mechanical^{41–44} and other computational simulations of model PFSA systems,^{45,46} which have been reviewed recently elsewhere.⁴⁷ Although atomistic and quantum mechanical simulations have been very helpful to clarify the mechanisms of side group aggregation and proton transfer in PFSA,^{44,48–50} they are less able to describe the morphology at a scale comparable with experimental SAXS data (5 to 200 nm) due to the relatively small number of atoms that can be considered and the long equilibration times required for the polymeric component. In this case, there are significant advantages in using mesoscale modelling techniques in which the atomistic structure is coarse-grained in some way, *e.g.* the ability to study much larger system sizes and use polymer chains with close to a realistic experimental molecular weight.⁵¹ So far, mesoscale simulations using a coarse-grained description for the ionomer structure, such as dissipative particle dynamics (DPD)^{51–54} or dynamic mean field theory (DMFT),^{55,56} have shown no direct evidence of either parallel channels or discrete spherical clusters in phase-segregated

morphologies. Instead, they tend to favour disordered structures in which continuous networks of ionic aggregates form as the water content is increased.

In the present work, we present results which demonstrate that the morphologies predicted by mesoscale DPD simulations are in quantitative agreement with the most likely distributions of charge density reconstructed from experimental SAXS data using maximum entropy techniques; *i.e.* the most statistically probable structural models for PFSA structure are also the most thermodynamically stable. First, the experimental methods and modelling techniques employed are briefly summarized below.

2 Methods

2.1 Experimental

SAXS data were recorded from Nafion 117 samples, in both the “as received” state (AR117) and after uniaxial tensile draw with extension ratio $L/L_0 = 1.5$ (“oriented” AR117). Orientation was conducted at an elevated temperature of 150 °C, just above the α relaxation temperature of the acid-form polymer. The SAXS data were obtained at the National Synchrotron Light Source (NSLS) at Brookhaven, using a wavelength of 0.137 nm, a sample-to-detector distance of 1.890 m and a detector pixel size of 158.0 μm . For a 1024×1024 pixel image, this gives a maximum scattering angle of $2\theta_{\text{max}} = \tan^{-1}(512 \times 158/1.89 \times 10^{-6}) = 2.451^\circ$. The calibration of detector pixel size and sample-to-detector distance was checked by using a silver behenate sample, which produced a peak with the expected Bragg spacing of 5.838 nm.

Water contents (expressed as $\lambda = \text{mol water/mol sulfonic acid groups}$) were in the range of $\lambda = 14$ to 16, corresponding approximately to exposure to fully saturated water vapour at 25 °C. However, during the SAXS data acquisition, samples were exposed to air for 85 s [sample loading time (25 s) + data acquisition time (60 s)], which makes it difficult to specify precise water uptake values. We have assumed $\lambda = 16$ (30 vol% H₂O for Nafion 117) in the DPD simulations.

2.2 Computational modelling

DPD simulations were carried out using a methodology described by Wu *et al.*⁵³ to generate several hundred independent configurations for a model Nafion PFSA ionomer with EW 1244 and water content $\lambda = 16$ (with chemical formula defined in Fig. 1 (c) in ref. 53). The DPD simulations were initialized using independently randomized bead positions and equilibrated for a period of up to 12 ns. Each simulation contained approximately 192 000 DPD beads, with radius 0.814 nm, corresponding to approximately 2.5 million atoms as defined by the coarse-grained representation described in ref. 53, and the dimension of simulation cell was 32.56 nm cubed. The interactions between the DPD beads were parameterized *via* classical atomistic MD simulations and hybrid density functional theory.

Maximum entropy (MaxEnt) reconstructions of charge density giving rise to 2D experimental small-angle X-ray scattering (SAXS) patterns were generated using a procedure first described by Elliott and Hanna,⁵⁷ and previously applied to SAXS data from PFSA ionomers.⁵⁸ Here, the diffraction data and real-space reconstructed charge distributions were represented by 8-bit 512×512 pixel images. Simulated SAXS patterns

were generated using a fast Fourier transform (FFT) technique, in which the scattered intensity $I(s)$ is given by:

$$I(s) = |R(s)|^2 = \iint_V \rho(\mathbf{r}')\rho(\mathbf{r}' - \mathbf{r})\exp(2\pi i\mathbf{r} \bullet \mathbf{s})d\mathbf{r}'d\mathbf{r} \quad (1)$$

where $R(s)$ is the structure factor in reciprocal space, $\rho(\mathbf{r})$ is the charge density in real space, and s is the scattering vector whose magnitude is given by $|s| = 1/d$ where d is the spacing given by the Bragg equation. Eqn (1) expresses the fact that the far-field Fraunhofer diffraction pattern is given by the Fourier transform of the autocorrelation of the charge density distribution, which, although mathematically indeterminate, can be inverted indirectly *via* application of the MaxEnt method. It is important to emphasize that the only input to MaxEnt algorithm is the experimental SAXS pattern, and no model for charge distribution is assumed *a priori*. The result is the most likely charge distribution that is consistent with the scattering data. Once the charge density distribution is obtained, the diffraction pattern can be derived straightforwardly as the squared complex modulus of the structure factor. This also allows for spatial filtering of the reconstructed charge densities by applying a Gaussian mask to the structure factor before carrying out the reverse Fourier transform. Since discrete Fourier transforms are used for the numerical calculations, the spatial resolution of the real space images is determined by the maximum scattering angle measured in reciprocal space. For a maximum scattering angle of $2\theta_{\max} = 2.451^\circ$ (see Section 2.1), the pixel resolution is given by $d_{\min} = \lambda/(2\sin \theta_{\max}) = 3.203$ nm for the real space images.

A similar procedure can be used to generate simulate SAXS from bead density distributions produced *via* DPD simulations. In principle, the full 3D scattering could be calculated from the DPD simulations; however, we chose to use a 2D cross-section of the 3D water bead density distributions in order to make an appropriate comparison between MaxEnt reconstructions of 2D experimental SAXS data and the DPD datasets. Since the morphologies predicted by DPD simulations turn out to be isotropic with respect to their orientation to the co-ordinate axes, there is no loss of information by carrying out 2D averaging in this way. In order to produce representative model structures with a real-space dimension equivalent to those resulting from the MaxEnt reconstructions from experimental data, it was necessary to construct montages from multiple independent DPD simulations. These were made by taking single cross-sections from each DPD simulation and placing it into a 2D array. In order to reduce artifacts resulting from such an ordered assembly, each image was rotated by a random integer multiple of 90° , and placed at a random position within the array. Despite the mismatch of densities at the boundaries of the individual component images, these montages give an overall convincing representation of the average structure of the PFSA model systems at a sufficiently large size scale to be able to meaningfully compare their 2D scattering to that of the experimental systems.

3 Results and discussion

3.1 “As received” Nafion AR117

Fig. 1(a) shows the unfiltered 2D MaxEnt reconstruction from Nafion AR117 after 10 000 iterations, together with the raw

experimental 2D SAXS data (top left, inset) and the simulated SAXS pattern of MaxEnt reconstruction (top right, inset). The simulated SAXS pattern of MaxEnt reconstruction is a good fit to the raw data, reproducing both the ionomer reflection occurring around $2\theta = 1.43^\circ$ and the lower angle reflection attributed to the fluorocarbon matrix. The remaining discrepancy is due to noise in the MaxEnt reconstruction, uncertainty concerning the absolute number of counts in experimental data, and the constraint of centrosymmetry in the simulated diffraction, which produces a spurious mirror image of the beam stop. Reconstructions from SAXS data with beam stop removed gave qualitatively identical results, and so the original data were retained. The scale bars in MaxEnt reconstructions were determined from the maximum scattering angle in the diffraction patterns, and the overall dimensions of the 512×512 pixel MaxEnt reconstructions are $1.64 \mu\text{m}$ square. The light and dark regions in the reconstructed image may be interpreted as areas of low and high charge density, or *vice versa*, since the diffraction pattern is invariant under contrast reversal by Babinet’s principle.⁵⁹ The structure appears very disordered, as might be expected by applying the MaxEnt criterion, but can be described as a network of small aggregates with low/high charge density, surrounded by channels of high/low charge density. It should be emphasized that the positions of these aggregates and channels are *not* random, since they produce interference giving rise to the SAXS reflections shown in Fig. 1 (insets).

In order to interpret the origin of experimental SAXS peaks, spatial filtering was applied to the MaxEnt reconstruction as described in Section 2.2. Fig. 1(b) shows the low-pass filtered MaxEnt reconstruction in Fig. 1(a) after contrast reversal, from which has been subtracted 30% of the original image in Fig. 1(a), again after contrast reversal. This shows more clearly the network of small aggregates, appearing as white dots and corresponding to areas of low/high charge density in Fig. 1(a), superimposed on a separate network of white, elongated channels, corresponding to areas of high/low charge density in Fig. 1 (a). Since the simulated diffraction pattern from low-pass filtered reconstruction [inset to Fig. 1(b)] shows only the lower angle diffraction peak, then the most reasonable interpretation of the MaxEnt reconstruction is of a network of small ionic aggregates with low charge density (white dots), giving rise to ionomer reflection at higher angles, surrounded by regions of higher charge density (elongated white structures), corresponding to amorphous fluorocarbon chains and crystallites, giving rise to lower angle reflection. This is similar to an earlier interpretation by Elliott *et al.*,⁵⁸ except that they did not resolve the peak at low angles and attributed the upturn in scattering intensity to the transform of the shape function of ionic cluster aggregates. In this case, the ionic phase and fluorocarbon phase form spatially distinct, but bicontinuous, networks.

Another very important point is that the images in Fig. 1 are reconstructed from 2D averaged scattering from through-thickness SAXS measurements from thin membrane samples, and thus represent only a projection of the actual 3D morphology. In the absence of fully 3D SAXS data, it is therefore difficult to distinguish between the images in Fig. 1 and similar 2D projections of the fibrillar or parallel cylinder models discussed earlier. However, if we postulate that the morphology is isotropic, then there is no reason to suppose that our reconstructed cross-section

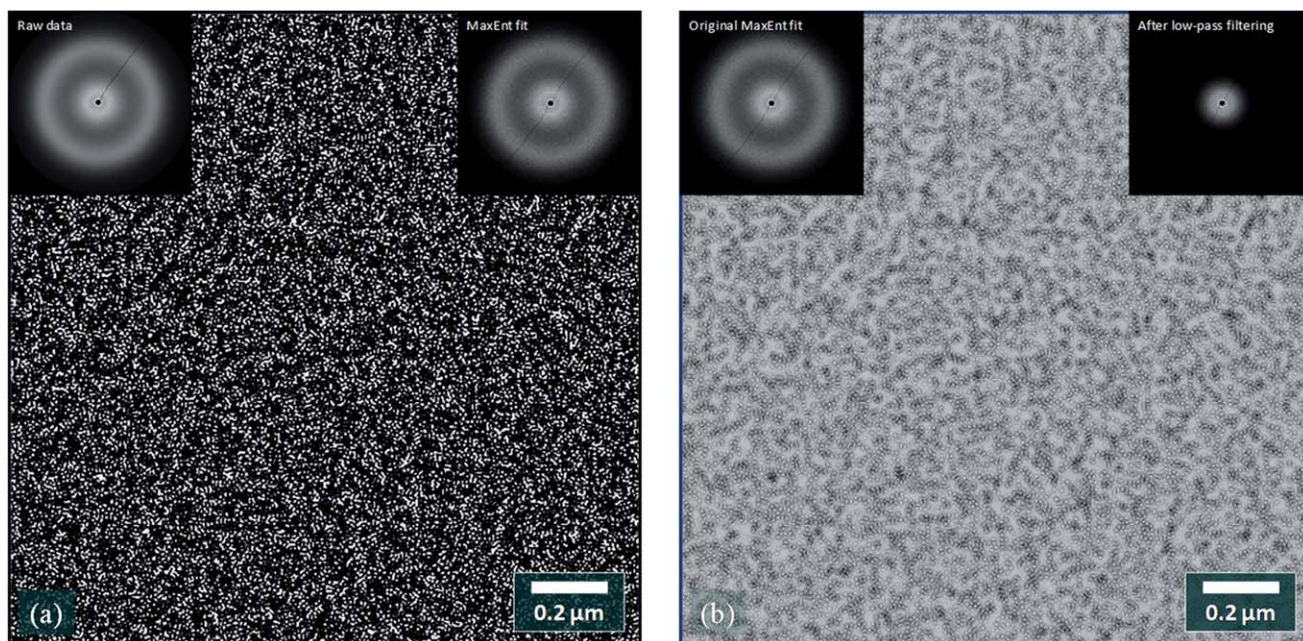


Fig. 1 (a) 2D MaxEnt reconstruction from AR117 SAXS data (shown in the top left inset, with MaxEnt fitted diffraction pattern shown in the top right inset) and (b) spatially filtered MaxEnt reconstruction of charge density from experimental small angle patterns (simulated SAXS data from original and filtered reconstructions shown in the top left and right insets, respectively).

is unique, and on that basis a schematic illustration of the 3D morphology proposed here is shown in Fig. 2. Although the representation is schematic, it is clear that any chosen 2D cross-section will closely resemble the images in Fig. 1. We now justify both the thermodynamic stability of such a model and its isotropy on the basis of comparison with computer simulations.

While the MaxEnt reconstructions presented in Fig. 1 give the most probable distribution of charge density consistent with the

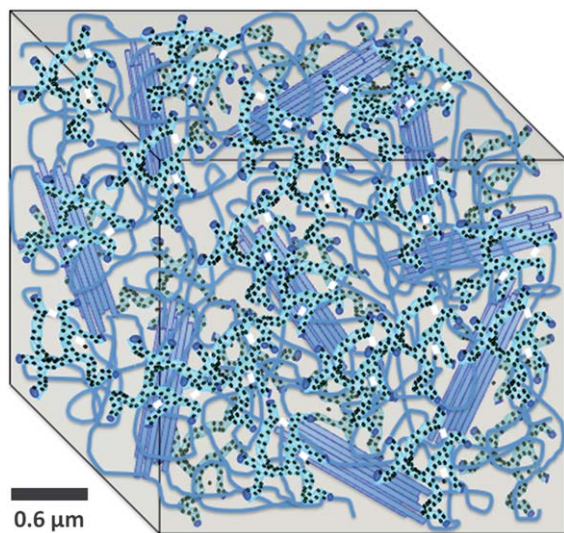


Fig. 2 Schematic representation of proposed morphology of hydrated Nafion, showing 3D continuous network (light blue channels) of ionic clusters (black dots) surrounded by amorphous and crystalline regions of fluorocarbon chains (dark blue). The scale bar is calibrated from the distance between ionic clusters (black dots) obtained from SAXS.

observed X-ray scattering, it is not necessarily the case that they correspond to the most thermodynamically stable structure when chemical information about chain connectivity and enthalpies of interaction between various components are taken into account. Furthermore, the assumption of an isotropic structure cannot be justified on the basis of SAXS data alone.

To this end, we have carried out dissipative particle dynamics (DPD) simulations, as described in Section 2.2, to generate the 3D model shown in Fig. 3(a). Although the structural properties of such systems as a function of water content and PFSA chemistry have been described in our previous studies,^{51,53} we focus here on 2D cross-sections of the water bead densities, such as shown in Fig. 3(b), where the white regions correspond to areas high in water bead density. By ignoring the densities of the fluorocarbon-containing beads, we have implicitly attributed to them a scattering density in contrast to the water beads, and it was found that using multi-phase models gave qualitatively very similar results. The major difficulty in comparing these cross-sections to the MaxEnt reconstructions is the large difference in size scale, since the dimensions of the DPD cell are only 33 nm compared to 1640 nm for the reconstructions. This was overcome by building montages from cross-sections obtained from multiple independent DPD simulations, as shown in Fig. 3(c), and described in Section 2.2. The cross-section in Fig. 3(b) is also shown, to the left side, reduced to the same scale as a montage of 121 independent cross-sections in Fig. 3(c) in order to give an impression of the change in scale. The linear dimension of the montage is 358 nm, and it represents the cross-section of a model with approximately 3×10^9 effective atoms.

Despite this change in scale, a 4×4 array of independently generated montages, such as the one shown in Fig. 3(c), were needed to enable direct comparison with MaxEnt reconstructions. Since the dimensions of the 4×4 DPD supercell image

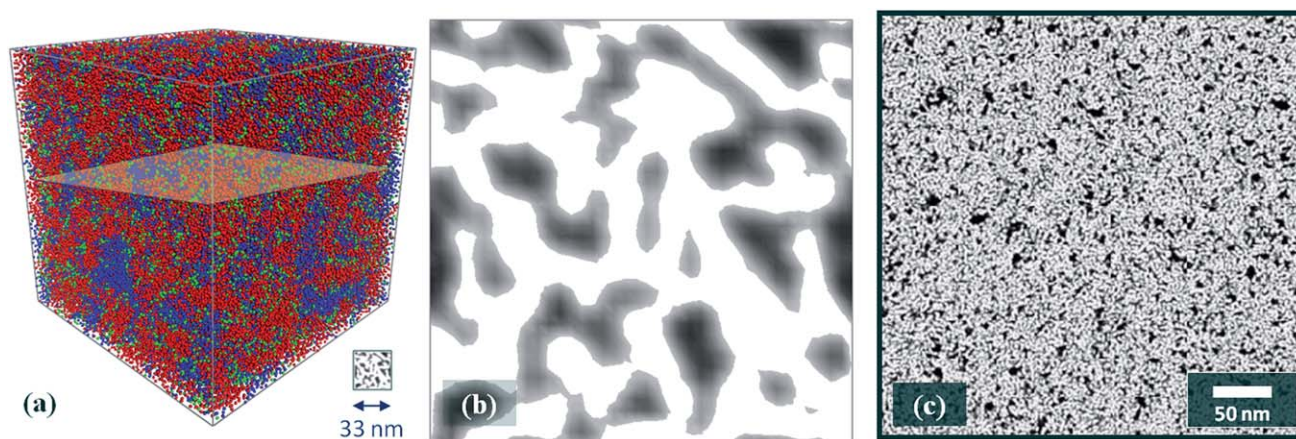


Fig. 3 (a) DPD simulation of Nafion ($EW = 1244 \text{ g mol}^{-1}$, $\lambda = 16$) with 3D distribution of fluorocarbon backbone beads shown in red, terminal portion of side chain beads in green and water beads in blue (full coarse-graining scheme described in ref. 53), (b) corresponding 2D cross-section, as highlighted in (a), of water bead density with white regions high in water content, and (c) 11×11 montage of 121 cross-sections through independently generated DPD simulations as in (a) produced from different random starting conditions. Note that the linear dimensions of (a) and (b) are 33 nm, and the inset shows cross-section (b) reduced to same scale as montage (c).

were $1.43 \mu\text{m}$ squared, a size reduction factor of $1.64/1.43 = 114\%$ was applied to the MaxEnt reconstruction, shown in Fig. 4 (a), in order to bring it into exact size correspondence with DPD image shown in Fig. 4(b). Both images have been spatially filtered by the same procedure used in Fig. 1(b) to enable a straightforward qualitative comparison of their features. The same network of water-rich ionic aggregates (white dots) and fluorocarbon channels (elongated white structures) can be seen in each image in Fig. 4, and their absolute sizes appear to correspond very well. However, the features in the DPD image are

more diffuse than those from the MaxEnt reconstruction, with some overlap between the ionic and fluorocarbon phases. This may be a result of the soft potentials used in the DPD simulations, or the spatial averaging used to produce the montages. However, since the DPD image contains approximately 2000 independent DPD cross-sections, corresponding to a structure with over 2×10^{11} effective atoms, it would be quite impossible to produce without some kind of spatial averaging.

In order to enable a quantitative comparison of the MaxEnt reconstruction and DPD images in Fig. 4, 1D scattering curves

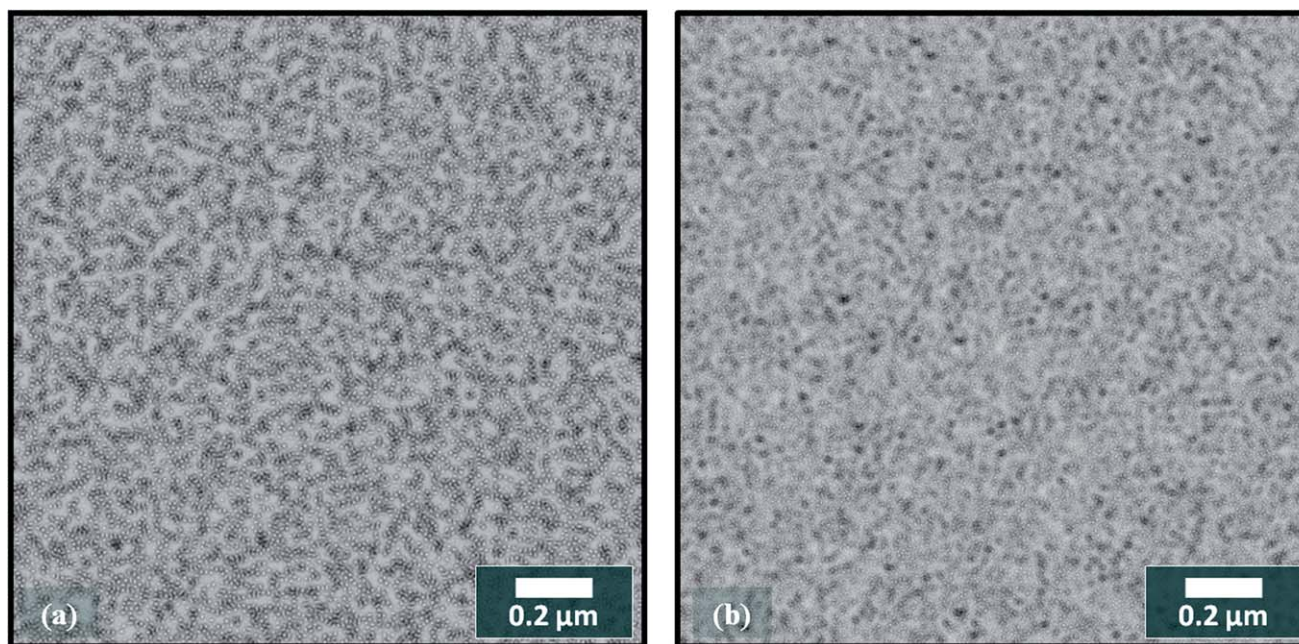


Fig. 4 Comparison of (a) 2D MaxEnt reconstruction from AR117 SAXS data (as shown in Fig. 1b, but rescaled and cropped in order to match dimensions of the DPD montage) and (b) montage of 2D water densities generated from the DPD simulations comprising of a 4×4 supercell of 16 independent instances of 11×11 montages of the type shown in Fig. 3(c). Both (a) and (b) have been spatially filtered to enhance contrast between water-rich ionic clusters (lighter dots) and fluorocarbon regions (lighter channels).

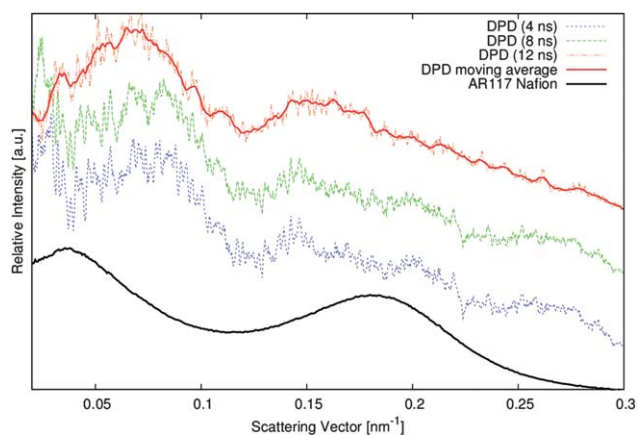


Fig. 5 Comparison of 1D-averaged simulated SAXS data (dashed lines) during DPD simulations (summed over 10 independent instances of water density montage), with red solid line showing 8-point moving average of data from DPD simulation after 12 ns, and 1D-averaged SAXS from AR117 Nafion (black solid line) used to fit the MaxEnt reconstruction.

were calculated by azimuthally averaging the 2D experimental results (fitted by MaxEnt) and simulated (DPD) SAXS patterns, as shown in Fig. 5. The SAXS patterns from DPD models were calculated sequentially at time intervals of 4, 8 and 12 ns in order to check the equilibration. Furthermore, scattering curves from 10 independent realizations of each model, with a single instance being shown in Fig. 4(b), were summed in an attempt to increase the signal-to-noise ratio. Although the SAXS data from the DPD model are still noisy, the general features of fluorocarbon and ionomer peaks are present in each simulated SAXS curve. At 4 and 8 ns, the ionomer peak is rather indistinct, whereas by 12 ns,

it peaks clearly around $s = 0.158 \text{ nm}^{-1}$ ($d = 6.3 \text{ nm}$) as compared with $s = 0.182 \text{ nm}^{-1}$ ($d = 5.5 \text{ nm}$) for the experimental data. The fluorocarbon peak occurs at higher $s = 0.068 \text{ nm}^{-1}$ ($d = 14.7 \text{ nm}$) in the DPD curve compared to $s = 0.037 \text{ nm}^{-1}$ ($d = 27 \text{ nm}$) for the experimental data. Given that the dimensions of the DPD cell are approximately 33 nm cubed, it is perhaps not surprising that the smaller features are reproduced more accurately.

Nevertheless, the existence of a second maximum related to a network of fluorocarbon phase in the DPD simulations confirms the interpretation of this reflection in MaxEnt image, and is also consistent with a simple calculation based on crystallite volume, estimated *via* the Scherrer equation from wide-angle X-ray scattering data, which gives a lower bound of 10 nm for the average distance between crystallites assuming they are uniformly distributed. The discrepancy in the spacing of this reflection compared to experimental data may be related to a lack of significant chain ordering in DPD simulations. Due to the scale of coarse-graining in the DPD simulations, it was not possible to observe crystallization of the fluorocarbon directly; however, it is likely that crystallites will be present in regions of high fluorocarbon bead density.

3.2 “Oriented” Nafion AR117

Since one of the principal arguments in favour of the randomly oriented cylindrical models over spherical aggregates is the absence of significant meridional intensity in the ionomer peak following tensile draw, the SAXS data from Nafion AR117 oriented by uniaxial tensile draw with extension ratio $L/L_0 = 1.5$ were analyzed. Fig. 6(a) shows the unfiltered MaxEnt reconstruction, together with 2D experimental and MaxEnt fitted diffraction patterns. The draw direction is vertical with respect to the images and, by comparison with Fig. 1(a), it can be seen that

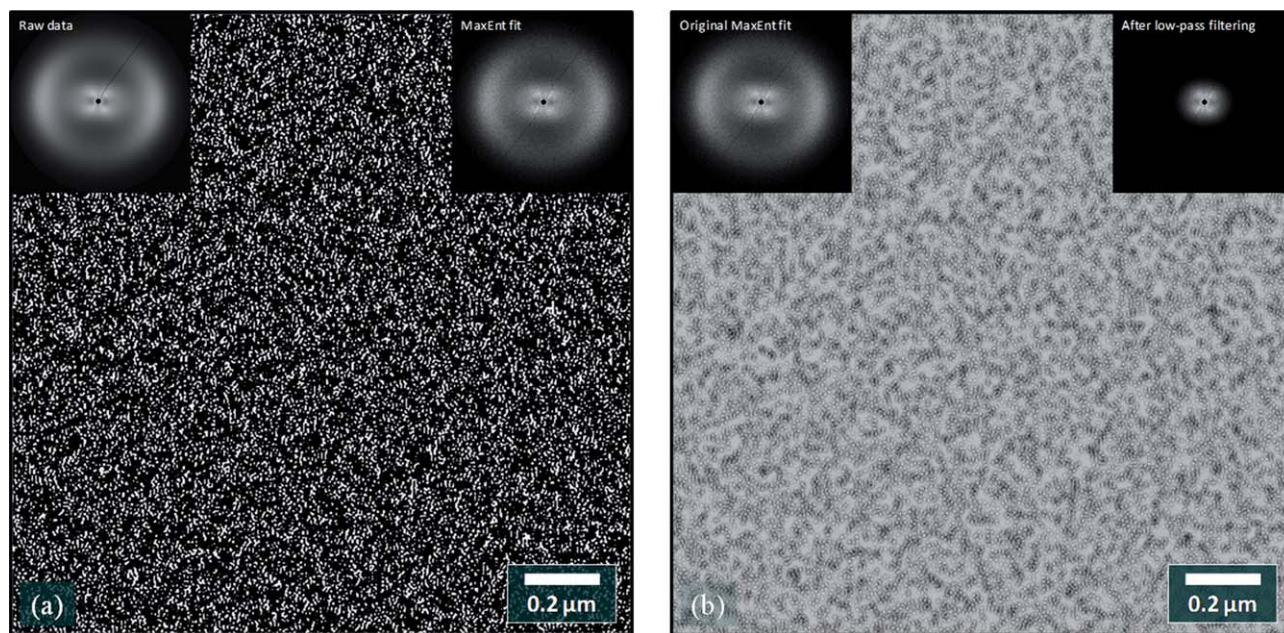


Fig. 6 (a) 2D MaxEnt reconstruction from uniaxially oriented ($L/L_0 = 1.5$) Nafion 117 SAXS data (shown in the top left inset, with MaxEnt fitted diffraction pattern shown in the top right inset) and (b) spatially filtered MaxEnt reconstruction of charge density from experimental small angle patterns (simulated SAXS data from original and filtered reconstructions shown in the top left and right insets, respectively). The draw direction is vertical.

the ionomer peak has strongly arced on the equator, while the fluorocarbon peak at lower angles has produced a “butterfly” four-point pattern⁶⁰ typical of oriented lamellar polymers.⁶¹ In this case, the scattering comes not from chain-folded lamellae, but from the contrast between fluorocarbon crystallites oriented obliquely to the draw direction and the lower density ionic regions. This can be seen more clearly in Fig. 6(b), showing the low-pass filtered MaxEnt reconstruction in Fig. 6(a) after contrast reversal, from which has been subtracted 30% of the original image in Fig. 6(a), again after contrast reversal.

The fluorocarbon-rich regions, represented by a network of white elongated channels, are preferentially oriented with spacings at approximately $\pm 38^\circ$ to the tensile axis, as compared with Fig. 1(b) where they are oriented isotropically. Their average separation has also increased slightly from 27 nm to 29 nm, whereas the spacings between ionic aggregates remained unchanged at 5.5 nm. Further orientation by tensile draw causes both fluorocarbon and ionomer peaks to concentrate strongly on the equator, with the spacing of former continuing to increase while the latter remains constant. This reinforces the interpretation that the ionic aggregates are intimately linked to, but spatially separate from, the larger scale organization of the fluorocarbon backbone, as shown in Fig. 2.

The loss of meridional intensity in the ionomer peak as a result of tensile draw has been attributed to changes in the spatial coherence of the network of ionic aggregates;⁵⁸ in other words, as the network of ionic clusters is stretched, the spacings between the aggregates become incoherent parallel to the draw direction relative to those in perpendicular direction. Although it is not possible to test this directly with DPD simulations presented here, they do confirm the interpretation of ionomer peak as arising from interparticle scattering from ionic aggregates. In particular, it is not necessary to invoke the orientation of extended cylindrical aggregates to explain the behaviour of ionomer peak.

4 Conclusions

Using a combination of statistical modelling to interpret SAXS data and coarse-grained DPD simulations of PFSA ionomers, it has been shown that the most plausible morphology consists of independent bicontinuous networks of ionic clusters and fluorocarbon chains. Although we are unable to observe fluorocarbon crystallites directly in the DPD simulations, the high density regions of fluorocarbon segments correspond exactly to regions where the density of ionic clusters is lowest. The model is consistent with SAXS from both unoriented PFSA membranes and those which have been subjected to tensile draw, and does not require the existence of extended parallel structures. The MaxEnt reconstructions are also qualitatively very similar to other disordered structure models (e.g. the clipped random wave approach of Aieta *et al.*⁶²) and demonstrate the problem of using structural models constructed *a priori* to interpret SAXS data, since a good match to scattering curve is only a necessary but not sufficient condition to establish the correctness of the model. In this case, additional information about both the statistical likelihood and thermodynamic stability of the model have been introduced, yielding a consistent morphology that agrees well with data using no direct fitting parameters on the scattering

data. In comparison to the cluster-network and fibrillar or parallel cylinder discussed earlier, it conforms exactly to none of them; however, it does retain the network of ionic aggregates found in the former and rejects the extended parallel channels found in the latter.

With respect to the relationship between morphology and transport properties, the existence of a continuous network of water-filled channels explains the high water diffusion coefficient of water in Nafion without the need for parallel channels. Furthermore, it allows for easy structural rearrangement *via* the redistribution of sulfonate groups between adjacent ionic aggregates upon water uptake, which is necessary to explain the non-affine macroscopic swelling behaviour when compared against the shift in the spacing of ionomer peak for an interparticle scattering model. It also suggests that, in order to facilitate the design of novel materials with improved performance over that of Nafion at low water contents, some means of sustaining the connectivity of these ionic clusters must be found. One possibility is the incorporation of inorganic nanoparticles containing ionic groups on their surface, which would limit the swelling and shrinkage of the membrane itself while maintaining a continuous network of bound water throughout the membrane. Such computational methods as DPD could be used in future to test new polymeric matrices and filler particles to establish their suitability in generating mesoscale morphologies for efficient proton conduction.

Acknowledgements

The authors acknowledge Dr Jong Keun Park for collecting the SAXS data for Nafion 117.

Notes and references

- 1 *Ionomers: Synthesis, Structure, Properties and Applications*, ed. M. R. Tant, K. A. Mauritz and G. L. Wilkes, Blackie Academic & Professional, Glasgow, 1997.
- 2 *Device and Materials Modeling in PEM Fuel Cells*, ed. S. J. Paddison and K. S. Promislow, Springer, New York, 2006.
- 3 C. Heitner-Wirguin, *J. Membr. Sci.*, 1996, **120**, 1–33.
- 4 K. D. Kreuer, *J. Membr. Sci.*, 2001, **185**, 29–39.
- 5 S. J. Paddison, *Annu. Rev. Mater. Res.*, 2003, **33**, 289–319.
- 6 K. D. Kreuer, S. J. Paddison, E. Spohr and M. Schuster, *Chem. Rev.*, 2004, **104**, 4637–4678.
- 7 J. Roziere and D. J. Jones, *Annu. Rev. Mater. Res.*, 2003, **33**, 503–555.
- 8 Q. F. Li, R. H. He, J. O. Jensen and N. J. Bjerrum, *Chem. Mater.*, 2003, **15**, 4896–4915.
- 9 D. J. Jones and J. Roziere, in *Fuel Cells I*, Springer-Verlag, Berlin, 2008, vol. 215, pp. 219–264.
- 10 B. F. Habenicht, S. J. Paddison and M. E. Tuckerman, *J. Mater. Chem.*, 2010, **20**, 6342–6351.
- 11 B. F. Habenicht, S. J. Paddison and M. E. Tuckerman, *Phys. Chem. Chem. Phys.*, 2010, **12**, 8728–8732.
- 12 C. Dellago, M. M. Naor and G. Hummer, *Phys. Rev. Lett.*, 2003, **90**, 105902.
- 13 T. E. DeCoursey, *Physiol. Rev.*, 2003, **83**, 475–579.
- 14 W. Y. Hsu and T. D. Gierke, *Macromolecules*, 1982, **15**, 101–105.
- 15 W. Y. Hsu and T. D. Gierke, *J. Membr. Sci.*, 1983, **13**, 307–326.
- 16 L. Rubatat, A. L. Rollet, G. Gebel and O. Diat, *Macromolecules*, 2002, **35**, 4050–4055.
- 17 K. Schmidt-Rohr and Q. Chen, *Nat. Mater.*, 2008, **7**, 75–83.
- 18 A. L. Rollet, O. Diat and G. Gebel, *J. Phys. Chem. B*, 2004, **108**, 1130–1136.
- 19 A. L. Rollet, O. Diat and G. Gebel, *J. Phys. Chem. B*, 2002, **106**, 3033–3036.

- 20 L. Rubatat, G. Gebel and O. Diat, *Macromolecules*, 2004, **37**, 7772–7783.
- 21 S. Schlick, G. Gebel, M. Pineri and F. Volino, *Macromolecules*, 1991, **24**, 3517–3521.
- 22 A. Guinier and G. Fournet, *Small-angle Scattering of X-Rays*, Wiley, New York, 1955.
- 23 G. Gebel and B. Loppinet, *J. Mol. Struct.*, 1996, **383**, 43–49.
- 24 P. Aldebert, B. Dreyfus, G. Gebel, N. Nakamura, M. Pineri and F. Volino, *J. Phys. France*, 1988, **49**, 2101–2109.
- 25 B. Loppinet and G. Gebel, *Langmuir*, 1998, **14**, 1977–1983.
- 26 G. Gebel, *Polymer*, 2000, **41**, 5829–5838.
- 27 D. E. Curtin, R. D. Lousenberg, T. J. Henry, P. C. Tangeman and M. E. Tisack, *J. Power Sources*, 2004, **131**, 41–48.
- 28 B. Chu, C. Wu and W. Buck, *Macromolecules*, 1989, **22**, 831–837.
- 29 O. Borodin, G. D. Smith and D. Bedrov, *J. Phys. Chem. B*, 2002, **106**, 9912–9922.
- 30 P. C. van der Heijden, A. de la Rosa, G. Gebel and O. Diat, *Polym. Adv. Technol.*, 2005, **16**, 102–107.
- 31 K. Schmidt-Rohr, *J. Appl. Crystallogr.*, 2007, **40**, 16–25.
- 32 P. C. van der Heijden, L. Rubatat and O. Diat, *Macromolecules*, 2004, **37**, 5327–5336.
- 33 K. A. Page, F. A. Landis, A. K. Phillips and R. B. Moore, *Macromolecules*, 2006, **39**, 3939–3946.
- 34 Q. Chen and K. Schmidt-Rohr, *Macromol. Chem. Phys.*, 2007, **208**, 2189–2203.
- 35 A. Kusoglu, M. H. Santare and A. M. Karlsson, *Polymer*, 2009, **50**, 2481–2491.
- 36 Y. A. Dyakov and Y. K. Tovbin, *Russ. Chem. Bull.*, 1995, **44**, 1186–1189.
- 37 J. A. Elliott, S. Hanna, A. M. S. Elliott and G. E. Cooley, *Phys. Chem. Chem. Phys.*, 1999, **1**, 4855–4864.
- 38 A. Vishnyakov and A. V. Neimark, *J. Phys. Chem. B*, 2001, **105**, 9586–9594.
- 39 S. S. Jang, V. Molinero, T. Cagin and W. A. Goddard, *J. Phys. Chem. B*, 2004, **108**, 3149–3157.
- 40 S. Urata, J. Irisawa, A. Takada, W. Shinoda, S. Tsuzuki and M. Mikami, *J. Phys. Chem. B*, 2005, **109**, 4269–4278.
- 41 S. J. Paddison and T. A. Zawodzinski, *Solid State Ionics*, 1998, **115**, 333–340.
- 42 S. J. Paddison, *J. New Mater. Electrochem. Syst.*, 2001, **4**, 197–207.
- 43 M. Eikerling, S. J. Paddison and T. A. Zawodzinski, *J. New Mater. Electrochem. Syst.*, 2002, **5**, 15–23.
- 44 S. J. Paddison and J. A. Elliott, *J. Phys. Chem. A*, 2005, **109**, 7583–7593.
- 45 P. G. Khalatur, S. K. Talitskikh and A. R. Khokhlov, *Macromol. Theory Simul.*, 2002, **11**, 566–586.
- 46 D. A. Mologin, P. G. Khalatur and A. R. Kholhlov, *Macromol. Theory Simul.*, 2002, **11**, 587–607.
- 47 J. A. Elliott and S. J. Paddison, *Phys. Chem. Chem. Phys.*, 2007, **9**, 2602–2618.
- 48 S. J. Paddison and J. A. Elliott, *Phys. Chem. Chem. Phys.*, 2006, **8**, 2193–2203.
- 49 S. J. Paddison and J. A. Elliott, *Solid State Ionics*, 2006, **177**, 2385–2390.
- 50 S. J. Paddison and J. A. Elliott, *Solid State Ionics*, 2007, **178**, 561–567.
- 51 D. S. Wu, S. J. Paddison and J. A. Elliott, *Macromolecules*, 2009, **42**, 3358–3367.
- 52 S. Yamamoto and S. A. Hyodo, *Polym. J.*, 2003, **35**, 519–527.
- 53 D. S. Wu, S. J. Paddison and J. A. Elliott, *Energy Environ. Sci.*, 2008, **1**, 284–293.
- 54 D. S. Wu, S. J. Paddison, J. A. Elliott and S. J. Hamrock, *Langmuir*, 2010, **26**, 14308–14315.
- 55 J. T. Wescott, Y. Qi, L. Subramanian and T. W. Capehart, *J. Chem. Phys.*, 2006, **124**, 134702.
- 56 D. Y. Galperin and A. R. Khokhlov, *Macromol. Theory Simul.*, 2006, **15**, 137–146.
- 57 J. A. Elliott and S. Hanna, *J. Appl. Crystallogr.*, 1999, **32**, 1069–1083.
- 58 J. A. Elliott, S. Hanna, A. M. S. Elliott and G. E. Cooley, *Macromolecules*, 2000, **33**, 4161–4171.
- 59 M. Born and E. Wolf, *Principles of Optics*, Pergamon Press, New York, 1980.
- 60 F. J. B. Calleja and C. G. Vonk, *X-Ray Scattering of Synthetic Polymers*, Elsevier, New York, 1989.
- 61 A. Cowking, J. G. Rider, I. L. Hay and A. Keller, *J. Mater. Sci.*, 1968, **3**, 646–654.
- 62 N. V. Aieta, R. J. Stanis, J. L. Horan, M. A. Yandrasits, D. J. Cookson, B. Ingham, M. F. Toney, S. J. Hamrock and A. M. Herring, *Macromolecules*, 2009, **42**, 5774–5780.